




# Machine Learning for Cloud Detection in IASI Measurements: A Data-Driven SVM Approach with Physical Constraints

Chiara Zugarini <sup>c,a,\*</sup>, Cristina Sgattoni <sup>b</sup>, Luca Sgheri <sup>a</sup>

<sup>a</sup>*CNR-IAC, Via Madonna del Piano, 10, Sesto Fiorentino, I-50019, FI, Italy*

<sup>b</sup>*CNR-IBE, Via Madonna del Piano, 10, Sesto Fiorentino, I-50019, FI, Italy*

<sup>c</sup>*Università di Firenze, Dipartimento di Ingegneria Informatica, Via di S. Marta, 3, Firenze, I-50139, FI, Italy*

---

## Abstract


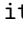

Cloud detection is essential for atmospheric retrievals, climate studies, and weather forecasting. We analyze infrared radiances from the Infrared Atmospheric Sounding Interferometer (IASI) onboard Meteorological Operational (MetOp) satellites to classify scenes as clear or cloudy.

We apply the Support Vector Machine (SVM) approach, based on kernel methods for non-separable data. In this study, the method is implemented for Cloud Identification (CISVM) to classify the test set using radiances or brightness temperatures, with dimensionality reduction through Principal Component Analysis (PCA) and cloud-sensitive channel selection to focus on the most informative features. Our best configuration achieves 88.30% agreement with reference labels and shows strong consistency with cloud masks from the Moderate Resolution Imaging Spectroradiometer (MODIS), with the largest discrepancies in polar regions due to sensor differences.

These results demonstrate that CISVM is a robust, flexible, and efficient method for automated cloud classification from infrared radiances, suitable for operational retrievals and future missions such as Far-infrared Outgoing Radiation Understanding and Monitoring (FORUM), the ninth European Space Agency Earth Explorer Mission.

---

\*Corresponding author. Email: chiara.zugarini@unifi.it

Email addresses: chiara.zugarini@unifi.it (Chiara Zugarini ) ,  
cristina.sgattoni@cnr.it (Cristina Sgattoni ) , luca.sgheri@cnr.it (Luca Sgheri )

*Keywords:* Cloud Detection, Machine Learning (ML), Principal Component Analysis (PCA), Support Vector Machine (SVM), Radiances, IASI

---

## 1. Introduction

Cloud cover is one of the most critical factors in atmospheric retrieval operations, as it significantly affects the quality and accuracy of atmospheric reconstruction models. Accurate cloud detection is essential not only for understanding atmospheric processes but also for improving climate and weather forecasting. Clouds play a fundamental role in Earth’s energy budget by both reflecting incoming solar radiation (producing a cooling effect) and trapping outgoing longwave radiation (producing a warming effect).

Cloud detection can be framed as a classification problem, making it well suited for Machine Learning (ML) approaches. In this study, we employ the Support Vector Machine (SVM) [1, 2, 3, 4], a well-established ML technique based on kernel methods, particularly effective for handling non-linearly separable data.

Our experiments are based on radiances acquired by the Infrared Atmospheric Sounding Interferometer (IASI) onboard the MetOp satellite [5, 6]. Scenes are classified according to the IASI Level 1C Cloud Cover (CC) field, which provides the percentage of cloud coverage within the instrument’s Field of View (FoV). Additionally, we incorporate soil type information from the ERA5 dataset [7], enabling data partitioning by soil type and, potentially, by climate zone based on scan geolocations.

We evaluated several preprocessing strategies, including the use of radiance or brightness temperature (BT), the latter compensating for variations in thermal emission. Dimensionality reduction is achieved either using Principal Component Analysis (PCA), or with selecting the channels most sensitive to cloud presence.

All experiments are performed on two seasonal periods: summer (June–July) and winter (December–January), to assess the impact of seasonality on classification performance.

This constitutes a self-consistency test, as accuracy is evaluated using the same parameter. To assess the reliability of the IASI L1 cloud cover we also compare the results of the classification with cloud information derived from the Moderate-Resolution Imaging Spectroradiometer (MODIS) instrument [8].

The results obtained are promising and contribute to a better understanding of the observed scenario, using only the information derived from infrared radiation. The accuracy in recognizing cloud cover is fundamental for improving atmospheric retrieval operations and for future applications in climate monitoring.

The paper is organized as follows. Section 2 provides general background on cloud detection from satellite data, outlining both traditional and machine learning-based approaches. Section 3 introduces the theoretical framework of Support Vector Machines (SVM), highlighting the role of kernel methods and their applicability to hyperspectral observations. Section 4 describes the construction of the training and test datasets from IASI L1C measurements, including the adopted thresholds and subdivisions. Section 5 presents the classification results obtained using SVM, evaluating the impact of different input representations (radiance and brightness temperature) and dimensionality reduction strategies, including PCA. Section 6 compares the SVM-based classifications with an independent cloud mask derived from MODIS observations. Finally, Section 7 summarizes the main outcomes of the study and discusses possible future developments.

## 2. Background

Accurate cloud detection from satellite observations is fundamental not only for preprocessing atmospheric parameters but also for numerical weather prediction and climate monitoring. Since the 1990s, operational algorithms based on multispectral thresholding, adaptive to surface type and illumination conditions, have been developed [9], achieving accuracy above 92% in mid-latitude regions.

Wavelet-based methods have been proposed as an auxiliary tool for cloud detection and classification from satellite images [10]. By applying 2D discrete wavelet transforms and discriminant analysis, the approach takes advantage of the spatial scale differences between clouds and surface features, enabling effective separation in the wavelet domain. However, no quantitative validation metrics were reported to assess classification performance.

McNally and Watts [11] introduced a physical approach based on the analysis of first-guess departures between observations and clear-sky simulations. This method allowed for the identification of clear channels even in partly cloudy scenes, with residual contamination below 0.2 K.

The Bayesian approach is another method for cloud detection. It was applied to Advanced Very High Resolution Radiometer (AVHRR) data by Heidinger [12]. The Pathfinder Atmospheres - Extended (PATMOS-x) dataset shows good agreement with MODIS products, despite differences in sensors and processing techniques. This suggests that different methods can still produce consistent cloud fraction estimates.

Stubenrauch [13] made an inter-comparison of cloud products obtained from different sensors, highlighting inter-instrument biases.

Supervised classification techniques such as Cumulative Discriminant Analysis (CDA) have been applied to IASI radiances to distinguish between cloudy and clear-sky observations in the thermal infrared [14]. The method used nine spectral statistics and a Principal Component Analysis (PCA) preprocessing step, achieving more than 80% agreement with AVHRR and Spinning Enhanced Visible Infra-Red Imager (SEVIRI) cloud masks on global and regional datasets.

The Cloud Identification and Classification (CIC) algorithm [15], based on PCA, is a machine learning method for cloud detection and scene classification using a univariate distribution and a similarity index threshold. It was tested on a large synthetic dataset covering a wide range of climatic conditions in the framework of the Far-infrared Outgoing Radiation Understanding & Monitoring (FORUM) End-to-End simulator project [16]. The method showed high detection rates for clear/cloudy scenes, particularly for thin cirrus clouds, and performance improved significantly when using far-infrared radiances, reaching detection scores up to 90%. However, performance tends to decrease in polar regions because of the reduced radiative contrast between clouds and the surface.

Supervised neural networks have also been used successfully: Mastro et al. [17] achieved 93% accuracy on IASI L1C spectral radiances, covering the period January 2016 to November 2016. The analysis was limited to specific geographic regions: Eastern Europe and tropical areas, where truth data were taken from a cloud mask product of the AVHRR. The methodology used a multilayer feedforward neural network trained on a subsampled dataset with well-known sky conditions, using PCA and regularization techniques to improve performance.

Recently, Whitburn et al. [18] used 45 selected IASI channels and reached 87% agreement with the operational IASI L1 radiances and L2 cloud product, creating a daily cloud mask using a supervised neural network (NN). The method was designed to ensure temporal consistency across the IASI time

series and different Metop platforms, avoiding channels affected by major absorption lines.

In the global context of using SVM for cloud detection, the application by Lee et al. [19] is particularly relevant. In their work, they applied Multicategory SVM (MSVM) to several simulated MODIS radiance channels, demonstrating the potential of this technique for satellite-based cloud classification, with the best recognition rate corresponding to a misclassification rate of 10.16%. Although the tests were limited in number and did not cover the entire globe, they clearly highlight the promise of this approach.

In the 2012 study by Addesso et al. [20], SVM were applied to cloud detection using multispectral images from the SEVIRI sensor. The method employed five spectral channels and introduced a penalty map to model spatial dependencies between pixels, enhancing classification performance. Their improved SVM-A approach achieved an overall accuracy of about 88.3%, demonstrating significant gains over classical SVM by reducing missed detections.

In the study by Murino et al. [21] in 2014, SVM were applied for cloud detection using multispectral MODIS data, including synthetic, expert-annotated, and real datasets. The SVM utilized multispectral radiance features to classify pixels, achieving success rates between 97.1% and 98.9% over land, and 98.3% to 99.2% over water. The study demonstrated that SVM, alongside k-Nearest Neighbors, provides high performance in cloud mask estimation from MODIS imagery.

Support Vector Machine has been effectively applied to classify cloud and land categories [22] using multispectral Landsat 8 imagery [23]. Training the SVM with both color and thermal channels achieved a high overall accuracy of 95.4%, highlighting the critical role of thermal radiance information in improving classification performance. These results demonstrate the strength of SVMs in leveraging radiance data for accurate cloud detection.

Maestri et al. [24] in 2019 applied SVM to downwelling far-infrared radiance measured by Radiation Explorer in the Far InfraRed Prototype for Applications and Developments (REFIR-PAD) over Antarctica, focusing on thin ice cloud classification. Unlike IASI, which observes upwelling radiance globally in the mid-IR from space, REFIR-PAD provides high-resolution ground-based measurements in the FIR. Their method relied on brightness temperature differences in the  $[380, 575]$   $\text{cm}^{-1}$  range, emphasizing local cloud microphysics rather than global-scale retrieval.

To the best of our knowledge, no direct applications of SVM to IASI

L1C spectral radiances have been reported in the literature. This study introduces the use of SVM for binary clear/cloudy classification from IASI L1C radiances, using sample subdivisions based on soil type and geographic location of the observed radiances. Future developments will aim to extend the method to multiclass cloud typing (ice, water, mixed clouds), leveraging the generalization capabilities of SVM in global scenarios.

Cloud coverage information is available in the IASI Level 1C products [6, 25], derived from the collocated AVHRR 1B radiometer. This parameter, expressed as a percentage, indicates the fraction of the IASI FoV obscured by clouds. The objective of this study is to develop a machine learning model capable of distinguishing clear and cloudy scenes directly from radiances, without relying on external instruments.

To better understand the classification approach adopted in this study, we briefly review the theoretical foundations of Support Vector Machines.

### 3. Support Vector Machine Theory

Support Vector Machines [1, 3] are supervised machine learning algorithms primarily used for classification tasks. Originally developed from the support vector method introduced by Vapnik in the 1960s, SVMs were later extended through kernel methods, which project the input data into a higher-dimensional feature space where the classes become linearly separable (i.e., separable by a hyperplane). The algorithm seeks the optimal separating hyperplane by maximizing the margin, defined as the distance between the hyperplane and the nearest data points from each class, known as support vectors.

Formally, given a training dataset of  $N$  labeled samples  $\{(\mathbf{x}_i, y_i)\}_{i=1}^N$  where  $\mathbf{x}_i \in \mathbb{R}^d$  and  $y_i \in \{-1, 1\}$ , SVM solves the following convex optimization problem:

$$\min_{\mathbf{w}, b, \xi} \frac{1}{2} |\mathbf{w}|^2 + C \sum_{i=1}^N \xi_i, \quad (1)$$

subject to:

$$y_i(\mathbf{w}^\top \phi(\mathbf{x}_i) + b) \geq 1 - \xi_i, \quad \xi_i \geq 0, \quad \forall i, \quad (2)$$

where  $\mathbf{w} \in \mathbb{R}^d$  is the normal vector of the separating hyperplane,  $b \in \mathbb{R}$  is the bias term and  $\phi : \mathbb{R}^d \rightarrow \mathcal{H}$  is a (possibly nonlinear) mapping into a higher-

dimensional feature space  $\mathcal{H}$ . For non-linearly separable data (i.e., data that cannot be perfectly divided by a straight hyperplane), slack variables  $\xi_i \geq 0$  are introduced to allow margin violations. The regularization parameter  $C > 0$  controls the trade-off between maximizing the margin and minimizing classification errors. This primal problem can be equivalently expressed in its dual formulation by introducing Lagrange multipliers, which allows the use of kernel functions to efficiently handle non-linear feature mappings:

$$\max_{\alpha} \sum_{i=1}^N \alpha_i - \frac{1}{2} \sum_{i=1}^N \sum_{j=1}^N \alpha_i \alpha_j y_i y_j K(\mathbf{x}_i, \mathbf{x}_j), \quad (3)$$

subject to:

$$\sum_{i=1}^N \alpha_i y_i = 0, \quad 0 \leq \alpha_i \leq C, \quad \forall i, \quad (4)$$

where  $K(\mathbf{x}_i, \mathbf{x}_j) = \langle \phi(\mathbf{x}_i), \phi(\mathbf{x}_j) \rangle$  is the kernel function that implicitly computes the inner product in  $\mathcal{H}$ .

Once the optimal multipliers  $\alpha_i$  are obtained, the decision function is expressed as:

$$f(\mathbf{x}) = \text{sign} \left( \sum_{i=1}^N \alpha_i y_i K(\mathbf{x}_i, \mathbf{x}) + b \right). \quad (5)$$

The dual formulation eliminates the need for an explicit feature mapping  $\phi$ , as inner products in  $\mathcal{H}$  are implicitly computed through the kernel function  $K$ , a property known as the kernel trick.

Commonly used kernels include:

- **Linear kernel:**  $K(\mathbf{x}_i, \mathbf{x}_j) = \mathbf{x}_i^\top \mathbf{x}_j$ ,
- **Polynomial kernel:**  $K(\mathbf{x}_i, \mathbf{x}_j) = (\mathbf{x}_i^\top \mathbf{x}_j + c)^d$ ,
- **Gaussian (RBF) kernel:**  $K(\mathbf{x}_i, \mathbf{x}_j) = \exp(-\gamma \|\mathbf{x}_i - \mathbf{x}_j\|^2)$ .

The choice of the kernel function determines the geometry of the feature space and strongly influences classification performance.

The polynomial kernel is particularly effective when the input features are correlated. By raising the inner product  $\mathbf{x}^\top \mathbf{x}'$  to the power  $d$ , it enhances the separation between classes by leveraging feature correlations in a higher-dimensional space. When two samples are strongly correlated, their

inner product is large, and the polynomial transformation further amplifies this relationship, improving the classifier’s ability to model complex class boundaries.

In contrast, the Gaussian kernel is more suitable for data with weaker correlations. Rather than relying on global correlations between features, it acts as a localized similarity measure, emphasizing proximity in the input space. It maps samples into an infinite-dimensional space where separability can be achieved even in cases of highly non-linear distributions.

To determine the most appropriate kernel for our application, we relied on the study conducted in [26], which investigated the influence of kernel choice on cloud detection using simulated hyperspectral data from the FORUM instrument [27, 28, 16], selected for launch as ESA’s ninth Earth Explorer mission [29].

This analysis demonstrated that the polynomial kernel outperforms other kernels when applied to hyperspectral radiances characterized by strong inter-channel correlations. This is consistent with the intrinsic spectral structure of instruments such as IASI, where radiances at adjacent wavenumbers are highly correlated. Consequently, in our experiments over continuous spectral ranges, we adopt the polynomial kernel. Conversely, when classification is performed using isolated and non-correlated channels, the Gaussian kernel is preferred.

Finally, SVM models are implemented using the `fitcsvm` function [30, 31] from the MATLAB programming environment, which provides efficient routines for training and cross-validating binary SVM classifiers on low- to moderately-dimensional datasets.

#### 4. Creation of Training and Test Sets from IASI Measurements

IASI [5] is a Fourier transform spectrometer onboard the MetOp satellites operated by the European Organisation for the Exploitation of Meteorological Satellites (EUMETSAT) and developed in cooperation with the European Space Agency (ESA), designed for atmospheric sounding in the infrared domain. It covers a swath of approximately 2200 km, corresponding to observation angles up to  $\pm 48.3^\circ$  from the nadir, enabling near-global coverage with successive orbits.

IASI measures radiances in the spectral range  $645\text{--}2760\text{ cm}^{-1}$  with a spectral resolution of  $0.5\text{ cm}^{-1}$ , and a spectral sampling of  $0.25\text{ cm}^{-1}$ . This high resolution allows for accurate retrieval of vertical profiles of atmospheric



temperature, humidity, and trace gases, essential for both weather forecasting and climate monitoring. The instrument also provides data sensitive to cloud cover and surface characteristics, making it particularly valuable for atmospheric composition and pollution studies.

The Cloud Cover (CC) parameter represents the percentage of the FoV affected by clouds. CC information is provided in the Level 1c IASI product [6, 25], derived from AVHRR 1B co-located within the IASI FoV.

The algorithm is tested using the IASI-L1 estimate. The cloud cover derived from AVHRR is normalized to the  $[0, 1]$  range, and a threshold of 0.1 is applied to distinguish clear (cloud fraction  $< 0.1$ ) and cloudy (cloud fraction  $\geq 0.1$ ) scenes. As already mentioned, we construct two separate datasets, corresponding to two different seasons: June–July and December–January.

#### 4.1. IASI training set

The training dataset is constructed from IASI observations collected in June, July, and December 2023, and January 2024, with the 32 selected orbits listed in Table 1. The spatial distribution of clear-sky and cloudy IASI observations is shown in Figure 1, where the top panel corresponds to June–July and the bottom panel to December–January.

June–July			December–January		
Start Date	Start Time	Start Orbit	Start Date	Start Time	Start Orbit
2023-06-30	22:29:57	24108	2023-12-31	22:20:54	26722
End Date	End Time	End Orbit	End Date	End Time	End Orbit
2023-07-01	23:50:53	24123	2024-01-01	23:41:58	26737
Total Number of Orbits: 16			Total Number of Orbits: 16		

Table 1: Summary of starting and ending IASI orbits used for the training set in June–July 2023 and December 2023–January 2024. The orbits are daily and consecutive over each 24-hour acquisition period.

#### 4.2. IASI test set

Test sets, detailed in Table 2, are prepared following the same criteria, using 14 orbits from January, June, July, and December of previous years. Figure 2 shows the spatial distribution of clear-sky and cloudy scenes, with the top panel corresponding to June–July and the bottom panel to December–January.

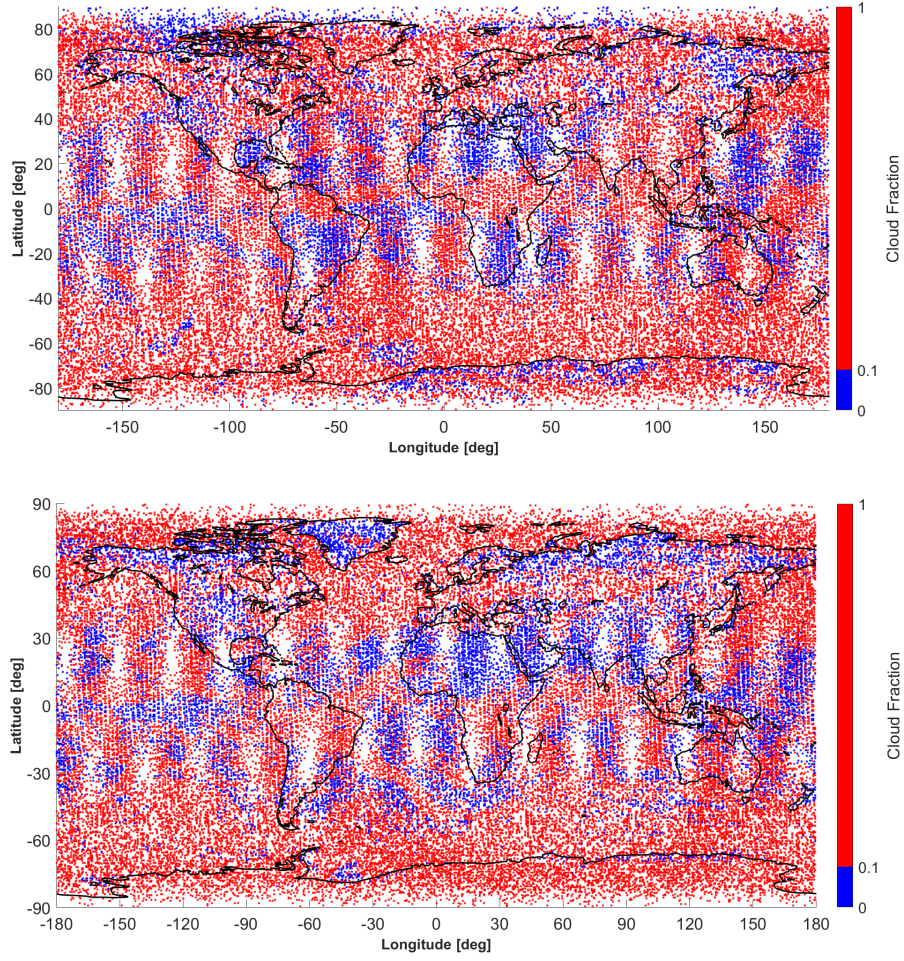


Figure 1: IASI clear-sky (blue) and cloudy (red) observations used for training: top panel refers to June-July 2023; bottom panel to December 2023-January 2024.

June–July			December–January		
Date	Starting hour	Orbit Number	Date	Starting hour	Orbit Number
2019-06-15	12:35:59	65662	2019-12-15	11:47:58	5732
2019-06-16	15:08:55	34991	2019-12-16	14:47:58	5748
2019-06-17	11:53:59	65690	2019-12-17	11:05:57	5760
2021-07-24	10:23:57	76600	2021-01-27	12:17:55	11543
2021-07-24	11:41:52	45914	2021-12-24	09:47:54	16244
2021-07-26	11:23:57	76629	2021-12-24	11:26:58	16245
2021-07-27	12:41:57	76644	2021-12-26	10:44:58	16273
Total Number of Orbits: 7			Total Number of Orbits: 7		

Table 2: Selected IASI orbits for the test set in June 2019, July 2021, and December 2019, January 2021, and December 2021.

#### 4.3. Additional information and sample subdivisions

In addition to the spectra, we add auxiliary surface information by using the soil type from the *ERA5 hourly data on single levels from 1940 to present* reanalysis dataset [7]. This variable reflects the texture of the terrain, which can affect surface emissivity and thus the radiance measurements. The different soil types used in this work are summarized in Table 3.

N.	Soil Type	N.	Soil Type
0	Non-land pixels	4	Fine
1	Coarse	5	Very Fine
2	Medium	6	Organic
3	Medium fine	7	Tropical Organic

Table 3: Description of soil type classes used in this work, based on ERA5 data.

Since ERA5 provides data on a fixed grid with  $0.25^\circ \times 0.25^\circ$  resolution, each IASI observation is assigned the soil type of the nearest each IASI observation is assigned the soil type of the nearest grid point in the  $L^1$  norm (based on latitude and longitude differences) with respect to the coordinates of the IASI FoV center. The global spatial distribution of soil types used in this study is shown in Figure 3.

Table 4 shows the total number of spectra contained in the training and test sets, divided by the periods of June-July and December-January, and by soil type.

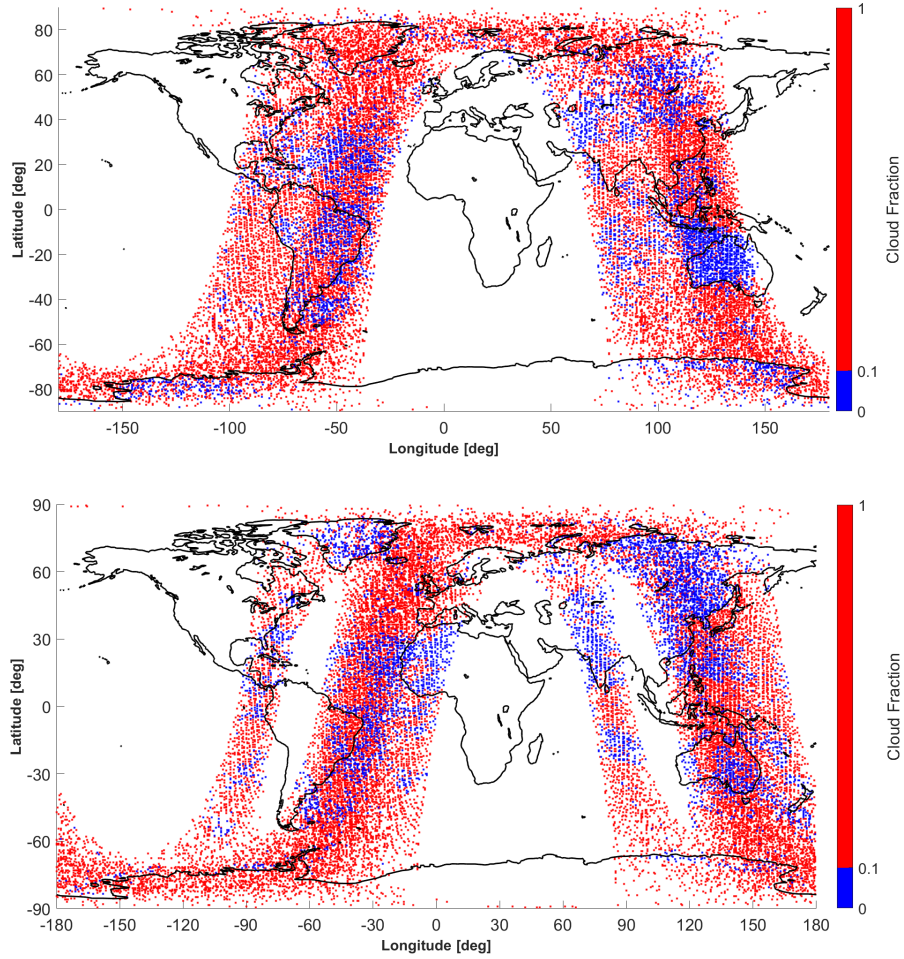


Figure 2: Spatial distribution of IASI clear-sky (blue) and cloudy (red) observations used for testing. The top panel refers to June 2019 and July 2021; the bottom panel refers to December 2019, January 2021, and December 2021.

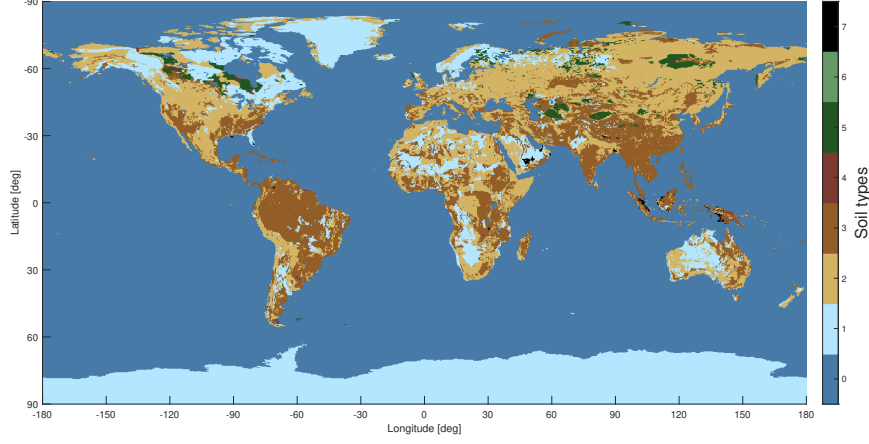


Figure 3: Global soil type map from ERA5. Each pixel represents the dominant soil texture at a spatial resolution of  $0.25^\circ \times 0.25^\circ$ .

June-July			December-January		
Soil Type	N. training sets	N. test sets	Soil Type	N. training sets	N. test sets
0	158344	61856	0	152840	70040
1	32016	15132	1	31216	12440
2	24836	11480	2	24388	11272
3	8336	6020	3	8000	3744
4	8172	6508	4	7040	3832
5	108	68	5	160	104
6	1964	984	6	1896	964
7	144	76	7	176	92
<b>TOTAL</b>	<b>232920</b>	<b>102124</b>	<b>TOTAL</b>	<b>225716</b>	<b>102488</b>

Table 4: Total number of spectra in the training and test sets for June–July and December–January, divided by soil type.

To study the impact of geolocation on the algorithm, we explore two dataset configurations with respect to climatic zoning:

- (a) No subdivisions: treating all data as one globally homogeneous set;
- (b) Climate zones: splitting the data into five latitudinal bands representing typical climatic regions: Tropical, Temperate North/South, and Polar North/South.

The latitude boundaries that define each subdivision are summarized in Table 5, while the corresponding global partitions are visualized in Figure 4.

Subdivision	Number of Area	Climate Zones	Latitude Range
No subdivisions	-	All	$[-90, 90]$
Climate zones	1	Tropical	$[-23, 23]$
	2	Temperate North	$[23, 66]$
	3	Temperate South	$[-66, -23]$
	4	Polar North	$[66, 90]$
	5	Polar South	$[-90, -66]$

Table 5: Latitude bounds defining the geographic subdivisions used in the preparation of training and test sets for cloud detection. The table includes two different geographic subdivisions: global (no subdivision) and five broad climate zones for spatially aware analysis.

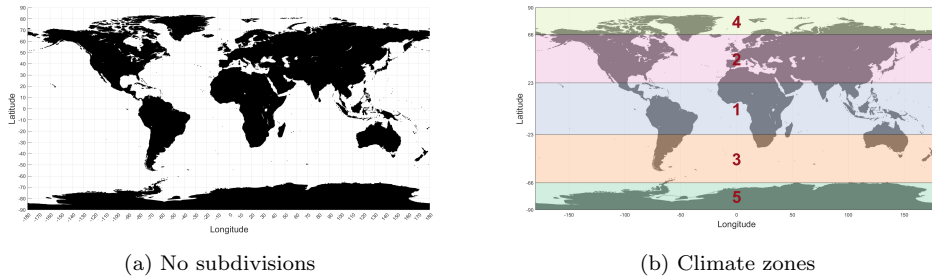


Figure 4: Geographic subdivisions applied to the dataset and test set. (a) No subdivision: the entire globe is treated as a single homogeneous region. (b) Climate zones: data are split into five latitudinal bands corresponding to tropical, temperate (north/south), and polar (north/south) regions.

The geographic and surface-type subdivisions are applied consistently to both training and test sets. Nevertheless, the algorithm’s performance is always evaluated in terms of global accuracy, defined as the overall percentage of correctly classified points across the entire test set.

## 5. Application of the algorithm to IASI measurements

To use the IASI spectra measurements, we set  $\mathbf{x}_i$  as the training set spectra in Equation (2), assigning the value  $y_i = 1$  if the  $i$ -th spectrum is clear and  $y_i = -1$  if the  $i$ -th spectrum is cloudy.

We use the MATLAB function `fitcsvm` [31] to create the separation using the training data, and the function `predict` [30] to obtain the classification

of each spectrum of the test set. The accuracy is then calculated as the percentage of correctly recognized spectra.

For simplicity, we refer to the algorithm described as the Cloud Identification SVM (CISVM).

In principle, the full IASI spectrum can be used as input for the SVM. However, spectral radiances are highly correlated. In the case of IASI, there is also spectral oversampling: the spectral step ( $0.25 \text{ cm}^{-1}$ ) is half the spectral resolution ( $0.50 \text{ cm}^{-1}$ ). To reduce dimensionality, several strategies can be adopted:

1. Select specific channels or spectral bands known from the literature to be particularly sensitive to cloud presence.
2. Apply Principal Component Analysis (PCA) to reduce dimensionality while retaining a large fraction of the variance captured in the training set.

Moreover, in both of these strategies, the radiance values can be replaced by brightness temperatures, defined as:

$$T_b(\nu) = \frac{hc\nu}{k} \left[ \ln \left( \frac{2hc^2\nu^3}{R(\nu)} + 1 \right) \right]^{-1} \quad (6)$$

where:

- $T_b(\nu)$ : Brightness temperature at wavenumber  $\nu$  [K]
- $\nu$ : Wavenumber [ $\text{cm}^{-1}$ ]
- $R(\nu)$ : Spectral radiance at wavenumber  $\nu$  [ $\text{W}\cdot\text{m}^{-2}\cdot\text{sr}^{-1}\cdot(\text{cm}^{-1})^{-1}$ ]
- $h$ : Planck's constant ( $6.626 \times 10^{-34} \text{ J}\cdot\text{s}$ )
- $c$ : Speed of light in vacuum ( $2.998 \times 10^8 \text{ m/s}$ )
- $k$ : Boltzmann constant ( $1.381 \times 10^{-23} \text{ J/K}$ )

The brightness temperature represents the temperature a blackbody would need in order to emit the same spectral radiance observed at a given wavenumber. In simple terms, it provides a way to normalize radiance with respect to the Planck function, facilitating physical interpretation.

A preliminary identification test using radiances is carried out to determine the most effective channel or band selection method for comparison with the PCA approach. This preliminary test accounts for geographic subdivisions and the division into soil types, as described in Section 4. Tests A to G are based on divisions of the main spectral regions within the IASI spectral range [32], where the term *primary application* denotes the principal use of each selected spectral band; meanwhile, Test H employs the channel selection proposed by Whitburn et al. [18], which consists of 45 IASI channels chosen for their sensitivity to cloud presence at various altitudes.

As described in Section 3, a polynomial kernel function is used for Tests A to G in Table 6, whereas a Gaussian kernel is adopted for Test H. In the former case, the selected bands include consecutive wavenumbers, resulting in strongly correlated radiance values. In contrast, Test H is based on individually selected channels that exhibit minimal mutual correlation, making the Gaussian kernel more appropriate. The results are reported in Table 6.



Test	Spectral Range or Selected Channels [cm <sup>-1</sup> ]	Primary Application	Total Rate Subdivision (a) N. Tests: 204612	Total Rate Subdivision (b) N. Tests: 204612
A	[645; 2760]	IASI range [32]	107844 52.70%	105372 51.50%
B	[800; 900]	Atmospheric Window	113884 55.66%	125376 61.27%
C	[770; 980]	Surface and cloud properties [32]	121684 59.47%	136384 66.65%
D	[1080; 1150]	Surface and cloud properties [32]	136808 66.86%	141520 69.17%
E	[2420; 2700]	Surface and cloud properties [32]	97196 47.50%	119488 58.40%
F	[770; 980] [1080; 1150]	Surface and cloud properties [32]	123612 60.41%	131248 64.14%
G	[770; 980] [1080; 1150] [2420; 2700]	Surface and cloud properties [32]	132872 64.94%	133080 65.04%
H	[826, 827.50, 861.50, 865.50, 866.25, 869.25, 871.25, 874.75, 877, 878.50, 880, 883.75, 885.75, 887.25, 891.25, 894.25, 897.75, 899.75, 901.50, 902.50, 905, 994.50, 996.25, 999.50, 1001.50, 1004.75, 1006.50, 1009.75, 1011.50, 1014.50, 2145.50, 2147.25, 2150, 2152.50, 2153.50, 2157.25, 2158.25, 2161.75, 2164.75, 2166.75, 2169.25, 2172.75, 2174.25, 2176.25, 2177.75]	IASI range with 45 selected channels [18]	157016 76.74%	150732 73.67%

Table 6: For each test type, the second and third columns report the selected spectral range or specific channels and their corresponding primary application. The last two columns show the total rate for subdivisions (a) and (b) as defined in Figure 4, including the total number of correctly classified points and the corresponding success rate (%) computed over the combined December–January and June–July test sets.

The best result from this preliminary test is achieved in Test H, highlighted in Table 6, yielding a classification accuracy of 76.74%. Since Test H yields significantly better results than all other configurations, its channel selection method is chosen for subsequent comparison with the PCA approach.

To evaluate the different strategies, we conduct eight tests resulting from the combination of the following three binary options:

- Soil type subdivision only (GLOBE) versus soil type combined with climatic zones (ZONES).
- Fixed channel selection (CHANNELS) versus principal component analysis (PCA).
- Radiance input (RAD) versus brightness temperature input (BT).

For PCA, we select a threshold of 0.995 on the captured variance to determine the number of principal components retained. It is worth noting that when using subdivisions based on both soil type and climatic zones, some combinations naturally result in empty subsets (e.g., *tropical organic* in *polar zones*). These cases pose no issue, as there are no corresponding data points in the dataset.

However, some subdivisions may contain only cloudy profiles in the training set. In principle, one could assign all test points to the only available class without applying the classifier, introducing no logical inconsistency. Nonetheless, a misclassification might occur in the unlikely event that clear-sky points appear in the test set. On the other hand, we adopt a more conservative approach and exclude such subdivisions from testing. This choice accounts for the slightly lower number of cases used in the ZONES tests.

BT or RAD	Geography Division	Spectral Domain	JUL	JAN	% TOTAL
BT	GLOBE	CHANNELS	88612/102124 86.80%	90064/102488 87.90%	178676/204612 87.32%
BT	ZONES	CHANNELS	87984/102064 86.20%	88704/102476 86.56%	176688/204540 86.38%
BT	GLOBE	PCA	90564/102124 88.78%	90032/102488 87.85%	180596/204612 88.26%
BT	ZONES	PCA	90308/102064 88.48%	89584/102476 87.42%	179892/204540 87.95%
RAD	GLOBE	CHANNELS	88112/102124 86.30%	89192/102488 87.03%	177304/204612 86.65%
RAD	ZONES	CHANNELS	88012/102064 86.23%	88428/102476 86.29%	176440/204540 86.26%
RAD	GLOBE	PCA	90668/102124 88.78%	90008/102488 87.82%	180676/204612 88.30%
RAD	ZONES	PCA	90128/102064 88.30%	89872/102476 87.70%	180000/204540 88.00%

Table 7: Cloud detection accuracy results using SVM for different physical quantities BT or RAD, for globe or climate zones divisions, and spectral input types for channels or PCA. Results are shown for July and January, with total performance on the right.

The results are shown in Table 7. To assess the statistical significance of the differences between test outcomes, we applied the z-test (see e.g. [33]) to pairs of tests. The corresponding significance levels are summarized in Table 8, where tests are identified by the initials of the first three columns of Table 7 and listed in decreasing accuracy order. Statistical significance is indicated as follows: ns (not significant), \* ( $p < 0.05$ , significant), \*\* ( $p < 0.01$ , highly significant), and \*\*\* ( $p < 0.001$ , very highly significant).

	RGP	BGP	RZP	BZP	BGC	RGC	BZC	RZC
RGP		ns	**	***	***	***	***	***
BGP			*	**	***	***	***	***
RZP				ns	***	***	***	***
BZP					***	***	***	***
BGC						***	***	***
RGC							*	***
BZC								ns
RZC								

Table 8: Significance of z-tests between test pairs: ns (not significant), \* ( $p < 0.05$ , significant), \*\* ( $p < 0.01$ , highly significant), \*\*\* ( $p < 0.001$ , very highly significant).

We note that most differences between tests are statistically significant, except for some tests that differ solely in the use of radiance versus brightness

temperature. Conversely, the most influential factor is the adoption of PCA: in all cases, replacing explicit channel selection with PCA leads to a very highly significant increase in classification accuracy.

We attribute this improvement to the fact that, while individual channels may exhibit enhanced sensitivity to clouds, the presence of clouds affects the entire spectrum by reducing the outgoing radiation measured by the instrument. Consequently, retaining most of the spectral variance enables a better separation of data points, albeit at the cost of an additional mathematical step, the singular value decomposition (SVD) used to compute the principal components. However, this step is required only during the training phase; for test samples, only a projection onto the precomputed components is needed.

Although the percentage differences in accuracy between tests are relatively small, their statistical significance is reinforced by the large sample size. This motivates us to select, for comparison with cloud cover data from a different instrument, the test configuration that achieves the highest accuracy.

## 6. Comparison with MODIS cloud mask

In the previous section, we evaluated the accuracy of the CISVM in classifying clear and cloudy spectra, using the IASI Level 1 cloud cover as the reference. That analysis solely assessed the model’s ability to replicate the same classification.

In this section, we compare the CISVM classification, specifically the configuration that yielded the highest accuracy (radiances, no climatic zones, and PCA), and the IASI Level 1 cloud cover itself against an independent cloud cover estimator.

In the following, the term *cloud mask* refers to a binary classification that indicates the presence or absence of clouds, in which each grid point is associated with a single cloud observation per day, thus representing the cloud conditions at that location and scan time.

For consistency, we retain the training set used for the best CISVM configuration. However, for the test set, we select an entire day of IASI measurements for each season, as detailed in Table 9.

December–January			June–July		
Start Date	Start Time	Start Orbit	Start Date	Start Time	Start Orbit
2022-01-21	23:32:55	16650	2022-07-18	23:50:57	19179
End Date	End Time	End Orbit	End Date	End Time	End Orbit
2022-01-22	23:11:59	16664	2022-07-19	23:29:53	19193
Total Number of Orbits: 15			Total Number of Orbits: 15		

Table 9: Summary of the starting and ending IASI orbits used for the test set in January 2022 and July 2022 for cloud mask generation. The orbits are daily and consecutive, covering each 24-hour acquisition period.

For comparison, we use data derived from the MODIS Level 2 cloud products [8]. MODIS instruments are onboard two different satellites: Terra and Aqua. By combining the MODIS Terra (MOD06\_L2) [34] and MODIS Aqua (MYD06\_L2) [35] datasets, we obtain two daily observations for each geolocation, thereby increasing the number of potential coincidences with IASI measurements.

Both datasets provide cloud mask information at a spatial resolution of 1 km. MOD06\_L2 corresponds to Terra’s morning overpass, while MYD06\_L2 refers to Aqua’s afternoon orbit, offering complementary temporal coverage.

We preliminarily test the CISVM algorithm on the newly selected IASI test set over the entire globe (i.e., prior to determining coincidences with the MODIS instrument), obtaining an accuracy of 87.13% in January and 88.22% in July, resulting in an overall accuracy of 87.67%. These values are very close to those obtained in the previous test, confirming the robustness of the CISVM method.

When comparing cloud products, a strict temporal threshold is necessary due to the highly dynamic nature of clouds. We set the coincidence threshold between MODIS and IASI measurements to 20 minutes, which is a reasonable value for cloud detection and for matching observations between the two sensors, while ensuring a sufficiently large test set.

Although all three satellites operate in sun-synchronous orbits, IASI and MODIS have different inclination angles, resulting in different orbital periods and longitudinal spacing between successive orbits. As a consequence, the number of coincidences depends on the selected day. The test days are chosen among those with the highest number of coincidences.

Coincidences between the IASI and MODIS orbits can be visually inspected using the orbit tracks and timing features available on the NASA Worldview website [36] for MODIS Aqua, MODIS Terra, and MetOp-C.

It is worth noting that, due to the different ascending node times, most coincidences along the orbit occur with the MODIS Terra satellite. MODIS Aqua contributes only a limited number of coincidences, primarily in the polar regions, which are sampled at every orbit.

Since MODIS data are provided on a 1 km grid, we identify all MODIS pixels falling within each IASI FoV and average their values to obtain a representative cloud fraction.

With this configuration, we obtain 1529 coincidences for the January test set and 2949 for the July test set.

Thus, we obtain the following three classifications on the same test set:

- **IASI-THR**: binary classification obtained by applying the threshold 0.1 using the IASI L1 cloud fraction data;
- **IASI-CISVM**: binary classification obtained using the CISVM algorithm trained on IASI L1 cloud fraction data and the same threshold;
- **MODIS-THR**: binary classification obtained by applying the same threshold 0.1 to MODIS cloud fraction data obtained from the MOD06\_L2 and MYD06\_L2 products.

Table 10 reports the percentage agreement for each pairwise comparison of these classifications, for both January and July.

<b>Dataset comparison</b>	<b>January</b>	<b>July</b>
IASI-THR vs MODIS-THR	76.85%	79.89%
IASI-THR vs IASI-CISVM	88.62%	89.01%
IASI-CISVM vs MODIS-THR	73.84%	80.91%

Table 10: Percentage agreement between the binary cloud classifications from the IASI-THR, MODIS-THR, and IASI-CISVM datasets for January and July.

From Table 10, we observe that the CISVM method maintains the high agreement of the IASI L1 classification, even on the reduced test set of matching points. The agreement between IASI-THR and MODIS-THR is relatively good; the differences can be attributed to the use of different instruments and methodologies to derive the cloud fraction.

A slightly lower agreement between IASI-CISVM and MODIS-THR is expected, as any misclassification by the CISVM model adds to the inherent

differences between the two instruments. This effect is visible as a slight degradation in accuracy for the January test set, whereas in July, the accuracy actually improves slightly.

Confusion Matrices – January			Confusion Matrices – July		
$\begin{bmatrix} 173 & 129 \\ 225 & 1002 \end{bmatrix}$	$\begin{bmatrix} 192 & 110 \\ 64 & 1163 \end{bmatrix}$	$\begin{bmatrix} 127 & 129 \\ 271 & 1002 \end{bmatrix}$	$\begin{bmatrix} 276 & 200 \\ 393 & 2080 \end{bmatrix}$	$\begin{bmatrix} 250 & 226 \\ 98 & 2375 \end{bmatrix}$	$\begin{bmatrix} 227 & 121 \\ 442 & 2159 \end{bmatrix}$

Table 11: Confusion matrices for January (left block) and July (right block). For each block: IASI-THR vs. MODIS-THR (left), IASI-THR vs. IASI-CISVM (center), and IASI-CISVM vs. MODIS-THR (right).

The confusion matrices in Table 11 for January and July show the level of agreement between pairs of classifiers: IASI-THR, MODIS-THR, and IASI-CISVM. Each matrix compares the outputs of two classifiers on the same dataset. The rows correspond to the predictions of the first classifier in the pair, while the columns correspond to those of the second classifier.

For each ordered pair (as specified in the table caption), element (1,1) indicates the number of points classified as *clear* by both classifiers, while element (2,2) indicates agreement on the *cloudy* class. Element (1,2) counts the number of points classified as *clear* by the first classifier and *cloudy* by the second, whereas element (2,1) represents the reverse situation.

Additionally, plots of the recognition differences amongst the three cloud masks are generated for January in Figure 5 and July in Figure 6. For each pair of datasets, the first is taken as the reference. In the plots, correctly classified cloudy points are shown in red, correctly classified clear points in blue, cloudy points misclassified as clear in violet, and clear points misclassified as cloudy in green.

It can be noted that the agreement between IASI and MODIS sensors is quite good in the tropical and temperate zones, while the agreement decreases in the polar zones. We report the original cloud fraction maps from IASI and MODIS for Antarctica in Figure 7. IASI detects a significantly higher cloud fraction, while MODIS reports clearer skies over the same locations and times. This discrepancy is consistent with the nature of the two sensors.

Cloud detection over Antarctica is challenging. Ice clouds and the snow-covered surface have similar radiative properties. This makes it hard for satellite sensors to distinguish between clear and cloudy scenes.

MODIS often underdetects clouds, especially during the polar night. This happens because its cloud detection relies on visible and near-infrared chan-

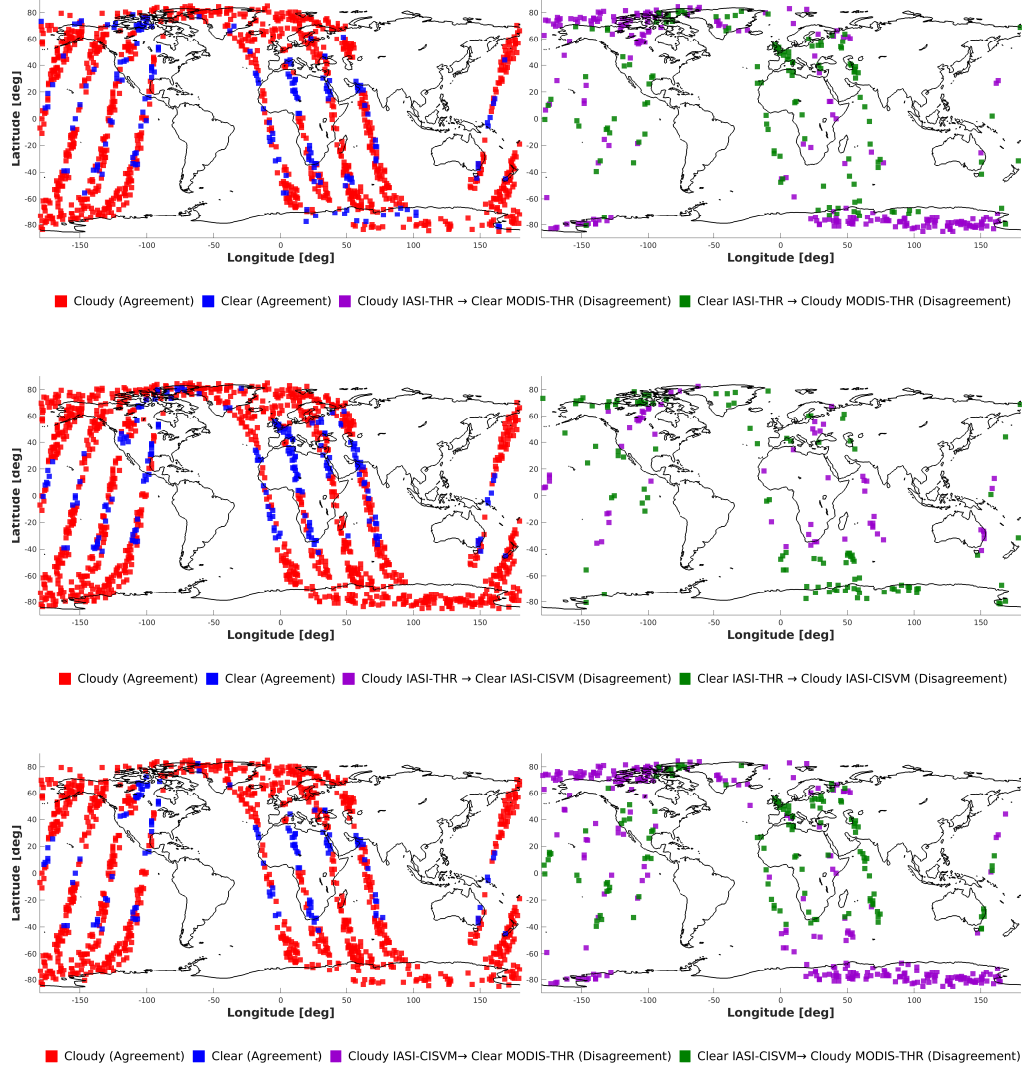


Figure 5: Differences in cloud detection agreement between the three cloud masks, at locations and times where all are available, for January 22, 2022. The figures in the panels are: IASI-THR vs MODIS-THR (top), IASI-THR vs IASI-CISVM (center), and IASI-CISVM vs MODIS-THR (bottom).



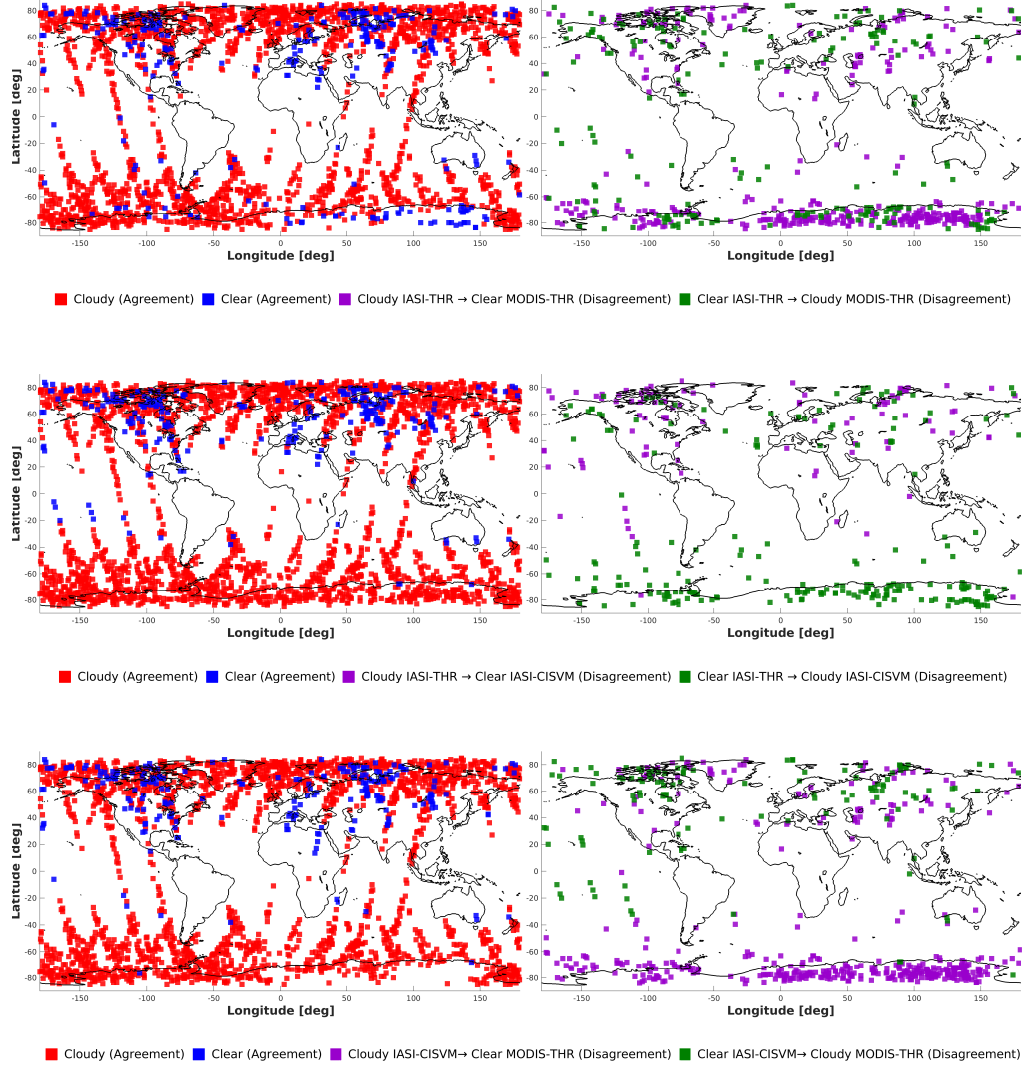


Figure 6: Differences in cloud detection agreement between the three cloud masks, at locations and times where all are available, for July 19, 2022. The figures in the panels are: IASI-THR vs MODIS-THR (top), IASI-THR vs IASI-CISVM (center), and IASI-CISVM vs MODIS-THR (bottom).

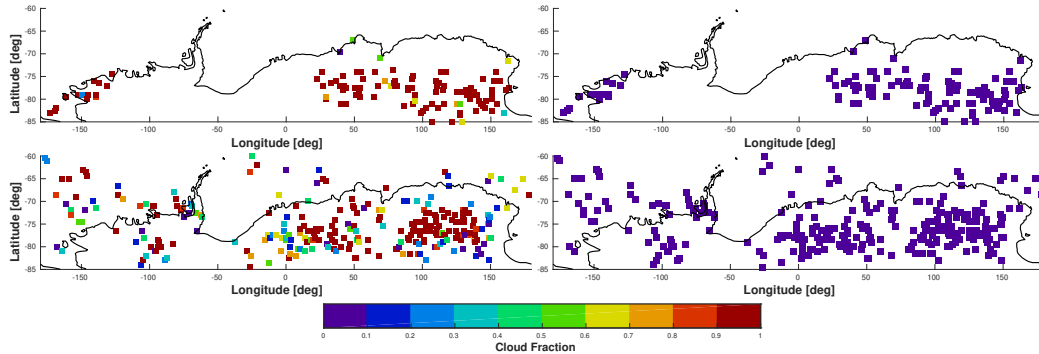


Figure 7: Cloud fraction over Antarctica corresponding to points classified as cloudy by IASI and clear by MODIS. The maps show the cloud fraction derived by IASI (left panels) and MODIS (right panels). Data for January 22, 2022, are shown on top, and for July 19, 2022, at the bottom.

nels. These channels do not work well without sunlight, so many cloudy scenes are classified as clear.

On the other hand, IASI tends to overdetect clouds. Brightness temperature differences, used by IASI to detect clouds, are sensitive to thermal inversions common in Antarctica. These inversions can lead to misclassification of clear-sky scenes as cloudy [37, 38, 39].

The L1C-AVHRR cloud product, included in IASI L1C data, also shows higher cloud detection over Antarctica. This confirms the general difficulty of detecting clouds in polar regions [18, 40].

It is widely acknowledged in the literature that thick clouds can be reliably detected from IASI radiances. However, detection accuracy decreases in two main situations.

First, for thin clouds, the radiance difference between clear and cloudy skies is minimal. FORUM simulations [16] have shown that clouds with an optical depth below  $0.03$  at  $900\text{ cm}^{-1}$  are generally undetectable, and this threshold increases to  $0.05$  when only the mid-infrared band is considered.

Second, in polar climatic zones, extremely low surface temperatures reduce the thermal contrast between the surface and the cloud top. This low contrast complicates cloud detection and can lead either to underdetection (as for MODIS during polar night) or to overdetection (as for IASI, due to its sensitivity to temperature inversions).

## 7. Conclusions

The SVM is a well-established and reliable method for classification. In this study, we proposed a machine learning approach, called CISVM, to detect clouds using IASI Level 1C infrared radiances. The main goal was to classify scenes as clear or cloudy directly from the spectra, without relying on additional instruments.

We tested several strategies. We used either radiances or brightness temperatures as input. Dimensionality reduction was applied in two ways: by selecting cloud-sensitive spectral channels or by using PCA. Training samples were divided by soil type. We also tested an additional subdivision by climatic zones.

All these methodologies resulted in small, albeit statistically significant, differences in agreement. The most significant improvement was achieved through the use of PCA. Using PCA on radiances, together with only the subdivision of samples by soil type, produced the best results. This approach reached an agreement of 88.30 % with reference cloud labels.

To compare the CISVM method with an independent cloud cover index, we used the MODIS Level 2 products from the Terra and Aqua satellites. Overall, the IASI and MODIS sensors have good agreement, except in the polar regions, where IASI detected more clouds than MODIS. The CISVM method, which relies only on radiances and geolocation, shows similar agreement with MODIS as the IASI Level 1C cloud product.

The SVM is a well-established machine learning technique for classification. In our opinion, the CISVM method still represents a robust, flexible solution for automatic cloud classification. Moreover, it is not dependent on additional instruments such as imagers to classify the scenes, so it can be applied to future instruments such as FORUM, where the imager will probably have a single channel, which will not be sufficient to reliably determine a cloud cover index.

The SVM method can also be extended to multiclass cloud classification (e.g., water, ice, mixed clouds), broadening its potential for more advanced use cases.

## Declarations

### *Funding*

NRRP (National Recovery and Resilience Plan) supported all authors under the project EMM (Earth-Moon-Mars, Mission 4, Component 2, In-

vestment 3.1, Project IR000038, CUPC53C22000870006).

*CRedit authorship contribution statement*

**Chiara Zugarini:** Methodology, Formal Analysis, Testing, Software, Writing – original draft, Writing – review & editing **Cristina Sgattoni:** Formal Analysis, Testing, Software, Writing – original draft, Writing – review & editing **Luca Sgheri:** Methodology, Formal Analysis, Writing – original draft, Writing – review & editing, Funding Acquisition;

*Conflict of interest*

The authors declare no conflict of interest.

## References

- [1] V. N. Vapnik, A. Y. Chervonenkis, A class of algorithms for pattern recognition learning, Vol. 25, 1964.  
URL <http://mi.mathnet.ru/at11678>
- [2] C. Cortes, V. N. Vapnik, Support-vector networks, Machine Learning 20 (3) (1995) 273–297. doi:10.1007/bf00994018.  
URL <https://doi.org/10.1007/bf00994018>
- [3] V. N. Vapnik, The support vector method of function estimation, Springer US, 1998, pp. 55–85. doi:10.1007/978-1-4615-5703-6\_3.
- [4] C. J. Burges, A tutorial on support vector machines for pattern recognition, Data Mining and Knowledge Discovery 2 (2) (1998) 121–167. doi:10.1023/a:1009715923555.  
URL <https://doi.org/10.1023/a:1009715923555>
- [5] D. Blumstein, G. Chalon, T. Carlier, C. Buil, P. Hébert, T. Maciaszek, G. Ponce, T. Phulpin, B. Tournier, D. Simeoni, P. Astruc, A. Clauss, Iasi instrument: Technical overview and measured performances, Proceedings of SPIE - The International Society for Optical Engineering 5543 (11 2004). doi:10.1117/12.560907.
- [6] EUMETSAT [online]. [link].

- [7] Hersbach, H., Bell, B., Berrisford, P., Biavati, G., Horányi, A., Muñoz Sabater, J., Nicolas, J., Peubey, C., Radu, R., Rozum, I., Schepers, D., Simmons, A., Soci, C., Dee, D., Thépaut, J.-N., ERA5 hourly data on single levels from 1940 to present. (2023). doi:10.24381/cds.adbb2d47.
- [8] C. O. Justice, J. R. G. Townshend, B. N. Holben, C. J. Tucker, et al., An overview of modis land data processing and product status, *Remote Sensing of Environment* 83 (1-2) (2002) 3–15. doi:10.1016/S0034-4257(02)00084-6.  
URL [https://doi.org/10.1016/S0034-4257\(02\)00084-6](https://doi.org/10.1016/S0034-4257(02)00084-6)
- [9] L. Lavanant, H. LeGléau, M. Derrien, S. Levasseur, G. Monnier, L. Ardouin, P. Brunel, B. Bellec, Avhrr cloud mask for sounding applications, in: J. Le Marshall, J. Jasper (Eds.), *Technical Proceedings of the 10th ATOVS Study Conference*, Bureau of Meteorology Research Centre, Melbourne, Australia, Boulder, Colorado, 1999, pp. 329–335.
- [10] U. Amato, G. Masiello, C. Serio, V. Cuomo, Cloud detection from satellite images by wavelets, Tech. report, Agenzia Spaziale Italiana (ASI), Roma, Italy, PDF available on CiteSeerX (2001).  
URL <http://citeseerx.ist.psu.edu/viewdoc/download?doi=10.1.1.20.4852&rep=rep1&type=pdf>
- [11] A. P. McNally, P. D. Watts, A cloud detection algorithm for high-spectral-resolution infrared sounders, *Quarterly Journal of the Royal Meteorological Society* 129 (595) (2003) 3411–3423. doi:10.1256/qj.02.208.  
URL <http://dx.doi.org/10.1256/qj.02.208>
- [12] A. K. Heidinger, A. T. Evan, M. J. Foster, A. Walther, A naive bayesian cloud-detection scheme derived from calipso and applied within patmos-x, *Journal of Applied Meteorology and Climatology* 51 (6) (2012) 1129–1144. doi:10.1175/jamc-d-11-02.1.  
URL <http://dx.doi.org/10.1175/JAMC-D-11-02.1>
- [13] C. J. Stubenrauch, W. B. Rossow, S. Kinne, S. Ackerman, G. Cesana, L. Di Girolamo, A. Gettelman, A. Guignard, A. Heidinger, H. Jacobowitz, et al., Assessment of global cloud datasets from satellites:

Project and database initiated by the gewex radiation panel, Bulletin of the American Meteorological Society 94 (7) (2013) 1031–1049. doi:10.1175/BAMS-D-12-00117.1.

- [14] U. Amato, L. Lavanant, G. Liuzzi, G. Masiello, C. Serio, R. Stuhlmann, S. A. Tjemkes, Cloud mask via cumulative discriminant analysis applied to satellite infrared observations: scientific basis and initial evaluation, Atmospheric Measurement Techniques 7 (10) (2014) 3355–3372. doi:10.5194/amt-7-3355-2014.  
URL <http://dx.doi.org/10.5194/amt-7-3355-2014>
- [15] T. Maestri, W. Cossich, I. Sbrolli, Cloud identification and classification from high spectral resolution data in the far infrared and mid-infrared, Atmospheric Measurement Techniques 12 (7) (2019) 3521–3540. doi:10.5194/amt-12-3521-2019.  
URL <http://dx.doi.org/10.5194/amt-12-3521-2019>
- [16] L. Sgheri, C. Belotti, M. Ben-Yami, G. Bianchini, B. Carnicero Dominguez, U. Cortesi, W. Cossich, S. Del Bianco, G. Di Natale, T. Guardabrazo, D. Lajas, T. Maestri, D. Magurno, H. Oetjen, P. Raspollini, C. Sgattoni, The forum end-to-end simulator project: architecture and results, Atmospheric Measurement Techniques 15 (3) (2022) 573–604. doi:10.5194/amt-15-573-2022.  
URL <https://amt.copernicus.org/articles/15/573/2022/>
- [17] P. Mastro, P. Pasquariello, G. Masiello, C. Serio, Cloud detection from iasi hyperspectral data: a statistical approach based on neural networks, in: A. Comerón, E. I. Kassianov, K. Schäfer, R. H. Picard, K. Weber, U. N. Singh (Eds.), Remote Sensing of Clouds and the Atmosphere XXV, SPIE, 2020, p. 11. doi:10.1117/12.2573326.  
URL <http://dx.doi.org/10.1117/12.2573326>
- [18] S. Whitburn, L. Clarisse, M. Crapeau, T. August, T. Hultberg, P. F. Coheur, C. Clerbaux, A  $\text{CO}_2$ -independent cloud mask from infrared atmospheric sounding interferometer (iasi) radiances for climate applications, Atmospheric Measurement Techniques 15 (22) (2022) 6653–6668. doi:10.5194/amt-15-6653-2022.  
URL <https://amt.copernicus.org/articles/15/6653/2022/>

- [19] Y. Lee, Y. Lin, G. Wahba, Multicategory support vector machines: Theory and application to the classification of microarray data and satellite radiance data, *Journal of the American Statistical Association* 99 (465) (2004) 67–81. doi:10.1198/016214504000000098.  
URL <http://dx.doi.org/10.1198/016214504000000098>
- [20] P. Addesso, R. Conte, M. Longo, R. Restaino, G. Vivone, Svm-based cloud detection aided by contextual information, in: 2012 Tyrrhenian Workshop on Advances in Radar and Remote Sensing (TyWRRS), 2012, pp. 214–221. doi:10.1109/TyWRRS.2012.6381132.
- [21] L. Murino, U. Amato, M. F. Carfora, A. Antoniadis, B. Huang, W. P. Menzel, C. Serio, Cloud detection of modis multispectral images, *Journal of Atmospheric and Oceanic Technology* 31 (2) (2014) 347–365. doi:10.1175/jtech-d-13-00088.1.  
URL <http://dx.doi.org/10.1175/JTECH-D-13-00088.1>
- [22] K. Wohlfarth, C. Schroer, M. Klab, S. Hakenes, M. Venhaus, S. Kauffmann, T. Wilhelm, C. Wohler, Dense cloud classification on multi-spectral satellite imagery, in: 2018 10th IAPR Workshop on Pattern Recognition in Remote Sensing (PRRS), IEEE, 2018, p. 1–6. doi:10.1109/prrs.2018.8486379.  
URL <http://dx.doi.org/10.1109/PRRS.2018.8486379>
- [23] NASA Landsat Program, Landsat 8 satellite, <https://landsat.gsfc.nasa.gov/satellites/landsat-8/>, accessed: 2025-07-20 (n.d.).
- [24] T. Maestri, C. Arosio, R. Rizzi, L. Palchetti, G. Bianchini, M. Del Guasta, Antarctic ice cloud identification and properties using downwelling spectral radiance from 100 to 1, 400 cm<sup>-1</sup>, *Journal of Geophysical Research: Atmospheres* 124 (8) (2019) 4761–4781. doi:10.1029/2018jd029205.  
URL <http://dx.doi.org/10.1029/2018JD029205>
- [25] EUMETSAT, IASI Level 1 Product Format Specification, Tech. Rep. EUM.EPS.SYS.SPE.990003, EUMETSAT (2011).  
URL [https://user.eumetsat.int/s3/eup-strap-media/pdf\\_iasi\\_level\\_1\\_pfs\\_2105bc9ccf.pdf](https://user.eumetsat.int/s3/eup-strap-media/pdf_iasi_level_1_pfs_2105bc9ccf.pdf)

- [26] C. Zugarini, L. Brugnano, L. Sgheri, Cloud detection using machine learning techniques with application to far and mid infrared measurements from the forum spectrometer., Master's thesis, Università degli Studi di Firenze, Firenze, Italia (2023).  
URL <https://sol.unifi.it/tesi/consultazione>
- [27] H. Oetjen, Report for mission selection: Forum, Tech. Rep. ESA-EOPSM-FORM-RP-3549, European Space Agency, ESA, 2200 AG, Noordwijk, The Netherlands (June 2019).  
URL <https://esamultimedia.esa.int/docs/EarthObservation/EE9-FORUM-RfMS-ESA-v1.0-FINAL.pdf>
- [28] L. Palchetti, H. Brindley, R. Bantges, S. A. Buehler, C. Camy-Peyret, B. Carli, U. Cortesi, S. Del Bianco, G. Di Natale, B. M. Dinelli, D. Feldman, X. L. Huang, L. C.-Labonnote, Q. Libois, T. Maestri, M. G. Mlynczak, J. E. Murray, H. Oetjen, M. Ridolfi, M. Riese, J. Russell, R. Saunders, C. Serio, Forum: Unique far-infrared satellite observations to better understand how earth radiates energy to space, Bulletin of the American Meteorological Society 101 (12) (2020) E2030–E2046. doi:10.1175/BAMS-D-19-0322.1.  
URL <https://doi.org/10.1175/BAMS-D-19-0322.1>
- [29] M. Ridolfi, S. Del Bianco, A. Di Roma, E. Castelli, C. Belotti, P. Dandini, G. Di Natale, B. M. Dinelli, L. C.-Labonnote, L. Palchetti, Forum earth explorer 9: Characteristics of level 2 products and synergies with iasi-ng, Remote Sensing 12 (9) (2020). doi:10.3390/rs12091496.  
URL <https://www.mdpi.com/2072-4292/12/9/1496>
- [30] MATLAB. Classify observations using support vector machine (svm) classifier [online].
- [31] MATLAB. Train support vector machine (svm) classifier for one-class and binary classification [online].
- [32] E. S. Agency, Spectral range, accessed: 2025-02-12 (2025).  
URL [https://www.esa.int/Applications/Observing\\_the\\_Earth/Meteorological\\_missions/MetOp/Spectral\\_range](https://www.esa.int/Applications/Observing_the_Earth/Meteorological_missions/MetOp/Spectral_range)
- [33] D. S. Moore, G. P. McCabe, B. A. Craig, Introduction to the Practice of Statistics, 7th Edition, W.H. Freeman and Company, New York, 2013.



- [34] MODIS Atmosphere Science Team, Modis/terra clouds 5-min l2 swath 1km and 5km (2017). doi:10.5067/MODIS/MOD06\_L2.061.  
URL [https://ladsweb.modaps.eosdis.nasa.gov/missions-and-measurements/products/MOD06\\_L2](https://ladsweb.modaps.eosdis.nasa.gov/missions-and-measurements/products/MOD06_L2)
- [35] MODIS Atmosphere Science Team, Myd06.l2 myd06.l2 modis/aqua clouds 5-min l2 swath 1km and 5km (2017). doi:10.5067/MODIS/MYD06\_L2.061.  
URL [https://ladsweb.modaps.eosdis.nasa.gov/missions-and-measurements/products/MYD06\\_L2](https://ladsweb.modaps.eosdis.nasa.gov/missions-and-measurements/products/MYD06_L2)
- [36] NASA Worldview, Nasa worldview - earth observing system data and information system (eosdis), <https://worldview.earthdata.nasa.gov/>, accessed: 2025-08-03 (2025).
- [37] R. E. Holz, S. A. Ackerman, F. W. Nagle, R. Frey, S. Dutcher, R. E. Kuehn, M. A. Vaughan, B. Baum, Global moderate resolution imaging spectroradiometer (modis) cloud detection and height evaluation using caliop, *Journal of Geophysical Research: Atmospheres* 113 (D8) (Apr. 2008). doi:10.1029/2008jd009837.  
URL <http://dx.doi.org/10.1029/2008JD009837>
- [38] Y. Liu, S. A. Ackerman, B. C. Maddux, J. R. Key, R. A. Frey, Errors in cloud detection over the arctic using a satellite imager and implications for observing feedback mechanisms, *Journal of Climate* 23 (7) (2010) 1894–1907. doi:10.1175/2009jcli3386.1.  
URL <http://dx.doi.org/10.1175/2009JCLI3386.1>
- [39] V. Volonnino, Cloud identification and classification from ground-based and satellite sensors on the antarctic plateau, Laurea magistrale thesis, Alma Mater Studiorum – Università di Bologna, Bologna, Italy (2023).  
URL <https://amslaurea.unibo.it/id/eprint/28476>
- [40] F. Donat, T. Maestri, E. Fabbri, M. Martinazzo, G. Bianchini, M. Del Guasta, G. Di Natale, L. Palchetti, G. Masiello, C. Serio, G. Liuzzi, Ground-based detection of antarctic clouds: analysis of cycles and comparison with iasi products (Jul. 2025). doi:10.5194/egusphere-2025-2793.  
URL <http://dx.doi.org/10.5194/egusphere-2025-2793>